Chemical Modification of 2D TMPTs

September 1, 2022 · salve-project.de/newspress/chemical modification of 2D TMPDs.html

September 1, 2022 – Transition metal phosphorus trisulfides (TMPTs) are layered materials with intrinsic magnetic properties. Researchers from Ulm University, the Helmholtz-Zentrum Dresden-Rossendorf and Aalto University have analysed in detail how the electron beam (30–80 kV) of the aberration-corrected SALVE microscope interacts with few-layer $MnPS_3$, $FePS_3$ and $NiPS_3$. Sulfur leaves first, oxygen moves in, and the defects add new states to the band gap, opening a way to tune ultrathin freestanding TMPTs by controlling their stoichiometry.

Some of the most intriguing magnets of the moment are only a few atoms thick. Two-dimensional (2D) materials already offer a wide range of fascinating electronic, optical and magnetic properties[1]–[4], and stacking individual layers creates heterostructures with properties of their own[5]–[7]. A promising family among them are the transition metal phosphorus trisulfides (TMPTs), layered compounds such as $MnPS_3$, $FePS_3$ and $NiPS_3$[8],[9]. Their band gaps span a wide range[10], from 1.5 to 3.0 eV[11],[12], and they consist mostly of earth-abundant, non-toxic elements[13], which makes them candidates for optoelectronics[14]. Above all, TMPTs are intrinsically magnetic: they are among the most recently studied antiferromagnetic 2D materials[15],[16], because their magnetic order survives down to a few layers[17], so they can serve as test beds for the fundamentals of 2D magnetism[13],[18]. Their layered structure also invites intercalation of ions or molecules[19], which makes them interesting for energy storage[20]–[22]; because lithium binds strongly to their surface, TMPTs have even been predicted to work as anodes in lithium-ion batteries[23].

Early theoretical and experimental work showed that the properties of these materials can be tuned. Under high pressure, for example, $MnPS_3$ and $MnPSe_3$ undergo a cooperative spin crossover and a semiconductor-to-metal transition[24]. Defects, however, had hardly been studied experimentally, although calculations for single layers predicted striking defect-induced changes in the electronic and magnetic properties, such as spin-split states inside the band gap of $MnPS_3$[25]. Several studies reported stacking faults in various TMPTs[26],[27] and showed that they strongly change properties such as the thermal conductivity[28], yet how defects act in few-layer systems remained open.

Transmission electron microscopy (TEM) is a particularly powerful tool here, because its fast electrons can modify[29],[30], probe[31]–[34] and individually address[35]–[39] the atoms of freestanding nanosheets. Aberration-corrected (AC) high-resolution TEM (HRTEM) correlates chemical and crystallographic information down to the atomic scale[40]–[42]. A prerequisite is clean, freestanding few-layer TMPT samples, which polymer-assisted mechanical exfoliation recently made possible[43]. What had been missing was a detailed study of how electrons in the low-voltage range of 30–80 kV, chosen to minimise damage[44], interact with these ultrathin crystals. A team from Ulm University, the Helmholtz-Zentrum Dresden-Rossendorf and Aalto University has now closed this gap for $MnPS_3$, $FePS_3$ and $NiPS_3$, combining Cc/Cs-corrected HRTEM, electron diffraction, energy-dispersive X-ray spectroscopy (EDX) and time-resolved electron energy-loss spectroscopy (EELS) with first-principles calculations.

Crystal structure and thickness analysis

The researchers first checked what they were looking at: the orientation, thickness and quality of the transferred pristine flakes, which are known to oxidise easily[43]. Because $MnPS_3$, $FePS_3$ and $NiPS_3$ share the same structure, the analysis of $MnPS_3$ holds for all three. In the bulk, the layers are stacked with a lateral shift and follow monoclinic symmetry[45] (Fig. 1a). All HRTEM images show the flakes viewed perpendicular to the layers, along the [103] direction (Fig. 1b). The best match to the experimental image is a simulated crystal of four layers without stacking faults, and an independent TEM thickness measurement[46] gives about 3 nm. The team concluded that the pristine samples are few-layer systems of 3–6 layers with very good crystal quality and no stacking faults; the box below explains how the image reveals this.

$MnPS_3$: reading structure and thickness from the image

Thin flakes were made by polymer-assisted exfoliation: bulk crystals were thinned with adhesive tape, pressed onto a silicon substrate coated with polyvinyl acetate, and floated with distilled water onto a Quantifoil TEM grid[43]. The flakes were clean, freestanding and could be imaged directly in the Cc/Cs-corrected SubÅngström Low-Voltage Electron Microscope (SALVE) at 30–80 kV.

In bulk $MnPS_3$ the monoclinic angle β is 107°[45] (Fig. 1a). Viewed along [103], the normal of the layer plane, the structure forms a centred rectangular pattern with a pronounced hexagonal pseudosymmetry. The unit cell contains six atomic rows along the b vector, and their composition alternates: rows 1 and 4 consist of S and P atoms, rows 2, 3, 5 and 6 of S and Mn atoms. This gives a 1:2 alternation of row contrast, which the line scans in Fig. 1b show directly. Electron diffraction confirmed that the flakes contain no stacking faults, and multislice image simulations of one to six layers identified the four-layer crystal in Fig. 1b. The thickness of about 3 nm from an EELS-based method[46] agrees with this result.

Interaction between electrons and sample

Under continuous irradiation the crystals give way layer by layer. Fig. 2 shows a four-layer $NiPS_3$ region that thins step by step, leaving areas of three, two and one layer. Single defects appear in the layers along the way: the 80 kV HRTEM images of single-

and double-layer $NiPS_3$ in Fig. 3a and 3b show isolated vacancies, marked by white arrows. In the double layer, the contrast at one site disappears, as the line scan in the inset of Fig. 3b shows; the defect is a sulfur vacancy (V_S) in an atomic column where the S atoms of the two layers sit on top of each other.

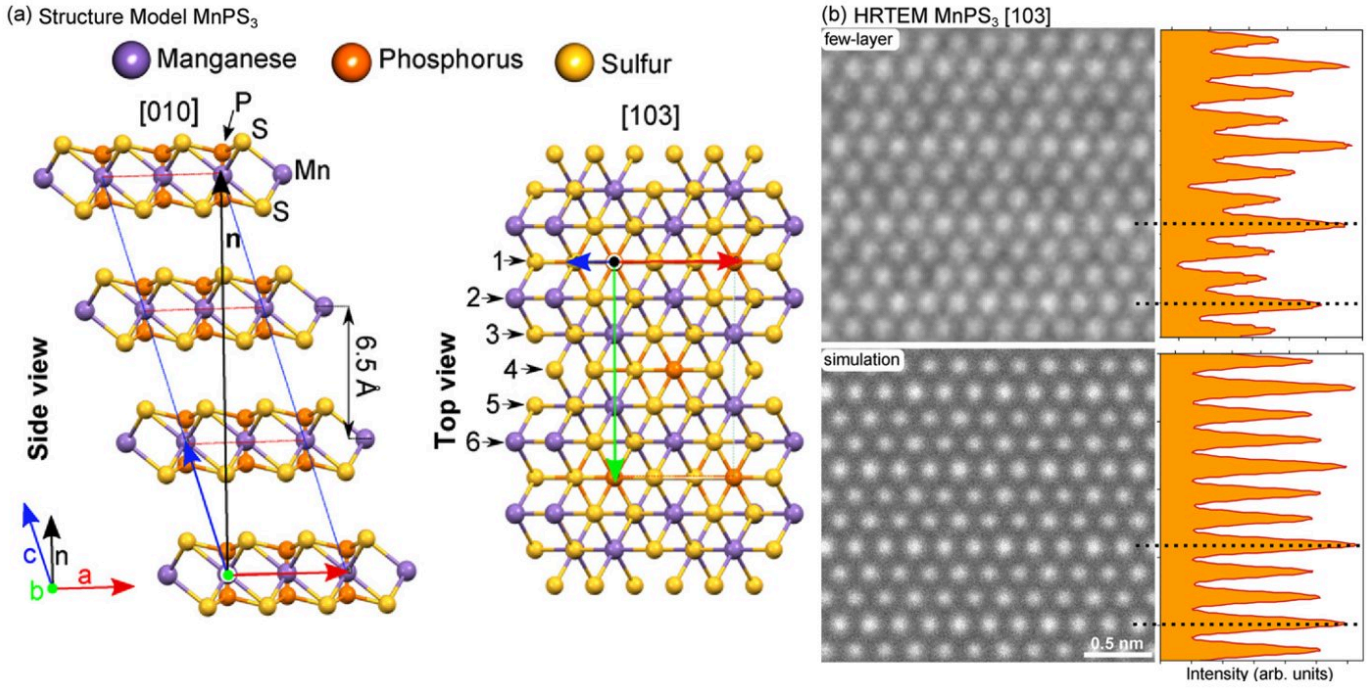

Fig. 1: Structure model of $MnPS_3$ and 80 kV HRTEM image of a four-layer flake with image simulation and line scans.

According to the experiments, sulfur or phosphorus vacancies form first and later grow into larger defects or even holes. To understand why, the team computed the displacement thresholds T_d of S and P atoms in single-layer TMPTs with ab initio molecular dynamics (Fig. 3c), as well as the cross sections for knock-on damage (Fig. 3d). The threshold for sulfur turned out to be clearly lower than that for phosphorus, and much lower than for graphene, so elastic collisions at 50–300 kV should remove more S than P. Inelastic scattering, known to matter in 2D insulators and semiconductors[47]–[50], adds further damage channels; in single-layer MoS_2 they create single S vacancies even at electron energies well below the knock-on threshold[47],[48],[51]. Since sulfur is also three times more abundant than phosphorus, the high-energy electrons (20–300 kV) should remove it easily, and strong structural changes are expected in few-layer systems as well. Imaging 2D materials entirely without beam–sample interaction may indeed be impossible[52]. The box below explains how the thresholds and cross sections were obtained.

TMPTs: displacement thresholds and cross sections

The displacement threshold T_d is the minimum kinetic energy a recoil atom must receive to leave its lattice site without recombining immediately. When the recoil points exactly along the surface normal, the leaving sulfur atom drags its nearest phosphorus neighbour along, and an S–P dumbbell is displaced. A single sulfur atom is sputtered only if its initial velocity deviates slightly from the normal, as happens when the beam is slightly tilted; this case is marked S* in Fig. 3c.

From these thresholds the team estimated the atomic displacement cross sections with the McKinley–Feshbach formalism[40],[53]–[55], taking lattice vibrations into account through a Debye model. Fig. 3d shows the resulting cross sections for S and P in $FePS_3$, $MnPS_3$ and $NiPS_3$[40],[49],[53],[56], with graphene as a reference that has a much higher threshold.

Defects also change what the material does electronically. Density functional theory (DFT) calculations showed that pristine TMPT single layers are semiconductors with band gaps of 2.0–2.3 eV, and that vacancies add new states in or near the gap (Fig. 4). Removing atoms is therefore a handle on the electronic properties, as the following box shows.

TMPTs: electronic structure of point defects

The optimised lattice constants of the pristine single layers agree very well with experiment and with earlier calculations[13]. The spin-polarised density of states (DOS) gives band gaps of 2.0–2.3 eV. Although a DFT band gap should not be compared directly with an optical gap[57], the PBE+U value for single-layer $FePS_3$ matches the measured 2.2 eV[12].

The team considered three types of point defects (Fig. 4): sulfur vacancies (V_S), phosphorus vacancies (V_P) and a combined S–P vacancy (V_{SP}). Sulfur vacancies introduce new spin-polarised states near the conduction and valence band edges, carried mainly by S p orbitals; in $MnPS_3$ these states merge into the band continuum. A single P vacancy creates localised states 0.2–0.7 eV

above the conduction band edge. The V_{SP} defect produces the most pronounced states and raises the electron density around the Fermi level, especially in $FePS_3$.

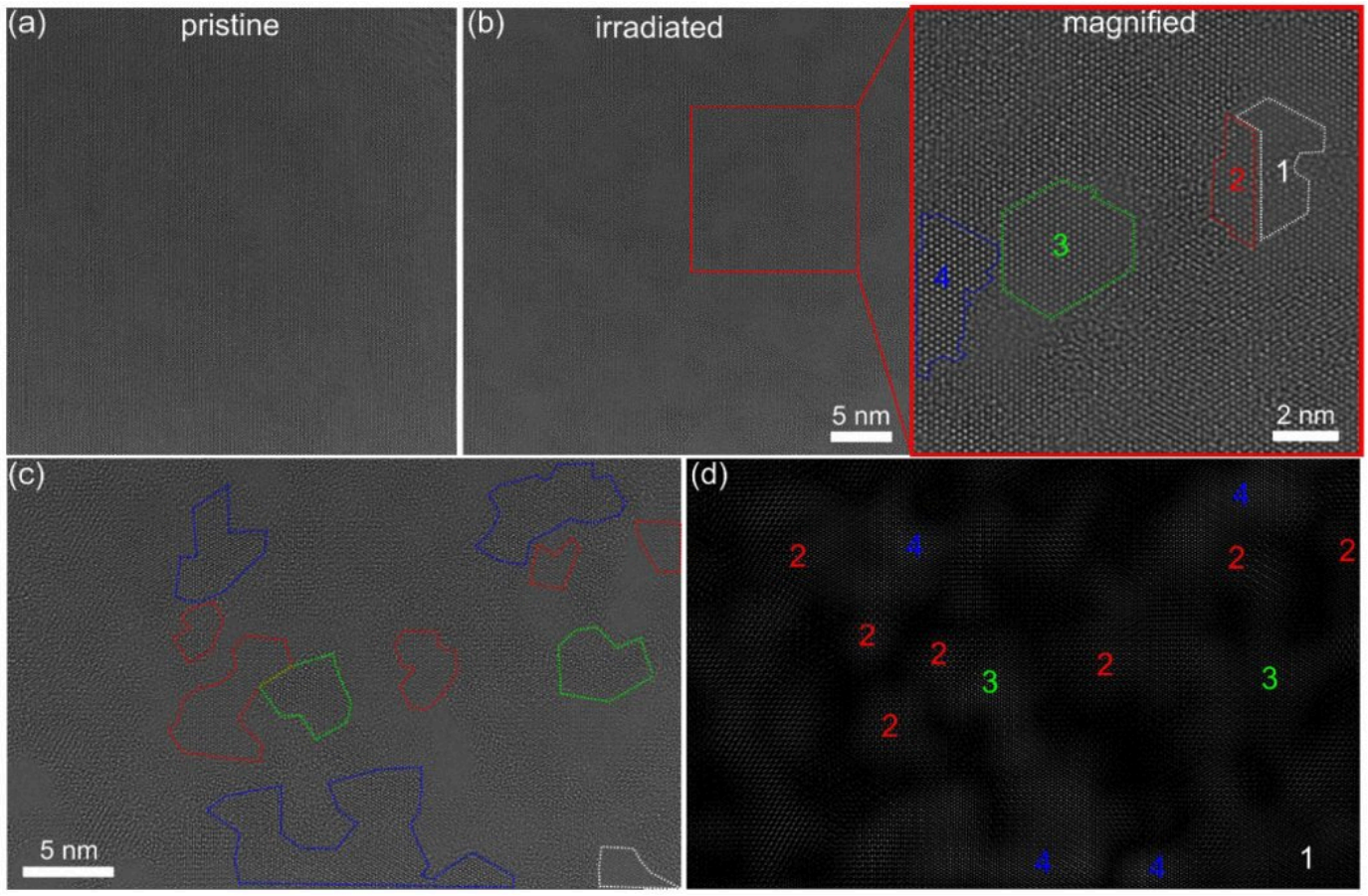

Fig. 2: 80 kV HRTEM of four-layer $NiPS_3$ before and after irradiation, with regions of one to four layers marked.

Electron beam excited chemical and structural changes analyzed with EELS and EDX

To follow the chemistry, the researchers looked in detail at $FePS_3$; $MnPS_3$ and $NiPS_3$ behaved in the same way unless noted otherwise. Fig. 5 shows an 80 kV high-angle annular dark-field (HAADF) image of an irradiated and an unirradiated region with the elemental maps of Fe, P, S and O. The irradiated region becomes disordered and forms clusters, as the magnified area in Fig. 5a and the HRTEM series in Fig. 6 show: first single atoms go missing, then the atomic columns deform, the crystal dissolves, holes open and the remaining material gathers into clusters. Comparing the atomic fractions of both regions confirmed that mainly sulfur is removed, in line with the calculations (Fig. 5b,c).

To compare with these images, the team modelled phases of intermediate stoichiometry that could form as sulfur is lost, by spreading vacancies evenly through the pristine structure as under prolonged irradiation. At sulfur vacancy concentrations above 50 %, the optimised structures showed the same clustering of metal atoms as the experiment. Such non-stoichiometric phases can be stabilised in the metal-rich regime, as shown earlier for transition metal dichalcogenides[58]. With more sulfur vacancies, the number of mid-gap states grew, and their position depended on how the defects were distributed. Eventually the states are expected to fill the whole band gap, so the irradiated samples may show hopping-type conductivity.

The conversion itself (Fig. 7a) was followed with the energy-loss near-edge structure (ELNES) of the core-loss edges, the fine structure that reveals bonding and oxidation states. The team recorded EELS spectra over 60 minutes at a constant, low dose rate of 15×10^3 $e^-/(s{\cdot}nm^2)$ and tracked how they evolved (Fig. 7). Both iron edges showed the same trend: the iron in pristine $FePS_3$ is mainly divalent (Fe^{2+}), as expected for this compound[59], and it gradually turned trivalent (Fe^{3+}) under the beam. At the phosphorus edge, the signal of the P–S bond faded and two new peaks appeared, while the phosphorus contributions grew relative to sulfur, again showing that mostly sulfur leaves. The box below explains how the edges were read.

$FePS_3$: reading the iron and phosphorus edges

The $M_{2,3}$ edge of first-row transition metals reveals their oxidation state[60]. Divalent iron shows a prominent pre-peak and a broad maximum near 57 eV; towards trivalent iron the main peak shifts to higher energy and the pre-peak weakens[60]. In pristine few-

layer $FePS_3$ the edge (Fig. 7b) looks mainly divalent[59]. With increasing exposure the main peak shifted and the pre-peak dropped strongly, best seen in Fig. 7c, where all spectra are aligned at 56.9 eV. The ratio of two 2.5 eV integration windows on the main peak and the pre-peak, w_M/w_P (Fig. 7d), rose from 1.7 (pristine) to about 2.8 (irradiated), indicating the change to Fe^{3+}[60]. An absolute Fe^{2+}/Fe^{3+} ratio cannot be given, because this universal curve[60] was calibrated only for high-spin iron oxides, and quantifying the valence from the intensity ratio alone is difficult[61].

The Fe $L_{2,3}$ edge (Fig. 7e) confirmed the result. After subtracting the background with a power-law model and the continuum with a double arctan function, the white-line ratio w_{L3}/w_{L2} was taken from two 2 eV windows at 709.5 and 720.9 eV (Fig. 7f). The L_3 peak shifted to higher energy and the ratio increased, showing the gradual change from Fe^{2+} to Fe^{3+}[62]–[65].

At the combined P and S $L_{2,3}$ edges (Fig. 7g), the pristine material shows a clear peak at about 132 eV (I) and a small one at 138.5 eV (II). The first agrees with earlier X-ray photoelectron spectroscopy (XPS)[16] and stems from P 2p transitions into the 3s σ* state of the S–P bond[16],[66]; the peak at 162 eV likewise comes from S 2p transitions[16],[66]. Under the beam the 132 eV peak decreased as the P–S bonds broke, and peaks at 138.5 eV (II) and 146.5 eV (III) appeared. The O K edge (Fig. 7h,i) grew steadily with exposure time.

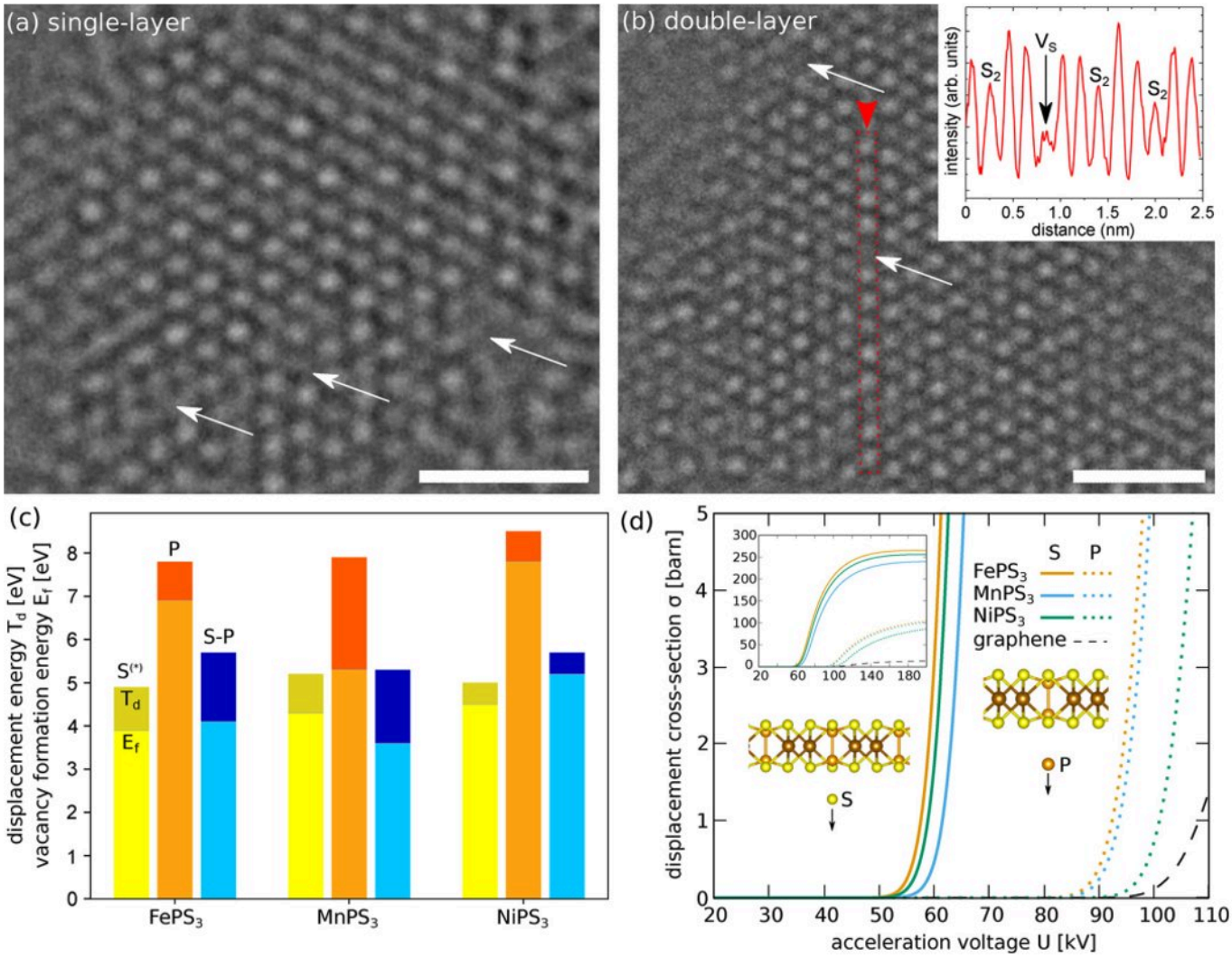

Fig. 3: HRTEM of vacancies in single- and double-layer $NiPS_3$, calculated displacement thresholds and knock-on cross sections.

The oxygen came from two sources: residual contamination on the surface and the residual gas in the microscope column, which the condensed beam ionises; even the carbon mesh of the TEM grid carries an oxygen signal. The damaged material is all the more prone to oxidation and pulls the oxygen towards the illuminated area, which matches the high oxygen content that EDX found there (Fig. 5). The new peaks at 138.5 and 146.5 eV fit earlier reports of P–O bonds in oxidised phosphorus compounds[67], so the accumulated oxygen binds to the remaining phosphorus, and together with the $Fe^{2+} \rightarrow Fe^{3+}$ shift in EELS (Fig. 7) and the EDX maps (Fig. 5) the data show oxygen bound to iron as well. The exact local stoichiometry and structure of the oxidised material could not be identified. Irradiation at 30 and 60 kV gave similar results for $MnPS_3$: again mainly sulfur and some phosphorus were removed, oxygen accumulated, and the residual P and Mn clustered together with O.

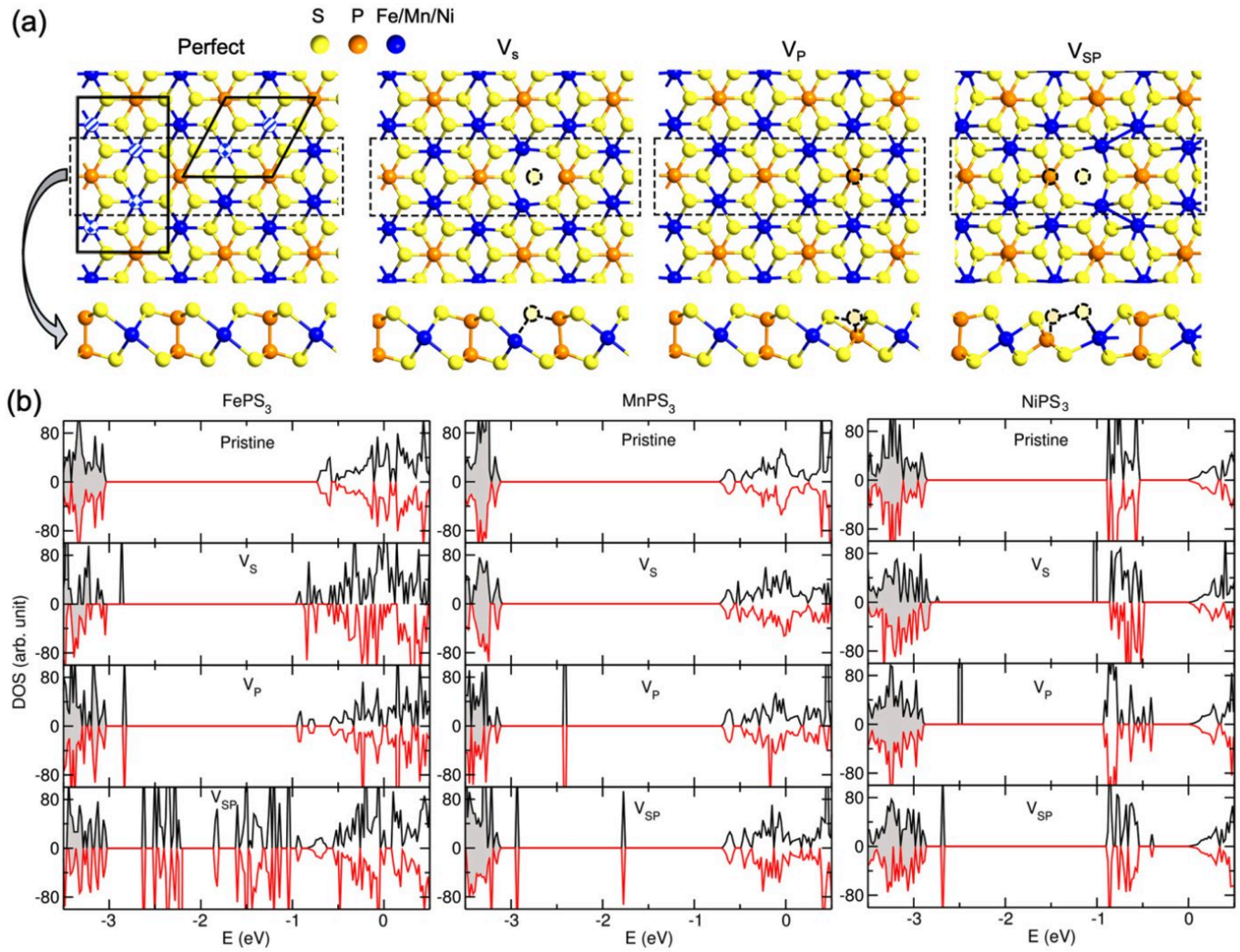

Fig. 4: DFT structures of S, P and S–P vacancies in single-layer TMPTs and their spin-polarised densities of states.

The study shows that ternary TMPTs have much lower knock-on thresholds than graphene and many binary transition metal dichalcogenides, that sulfur leaves first, and that the resulting vacancies add new states to the band gap and, depending on the sulfur content, magnetism from asymmetric spin polarisation. The experiments also illustrate, as the authors write, “the sensitivity of TMPTs to oxidation and the necessity to control the imaging conditions (i.e., dose rate as well as the irradiation time).” Controlled at the atomic scale in the Cc/Cs-corrected SALVE microscope at Ulm University, the electron beam thus becomes a tool: by setting how much sulfur remains, it opens a way to tailor the electronic and structural properties of freestanding few-layer TMPTs.

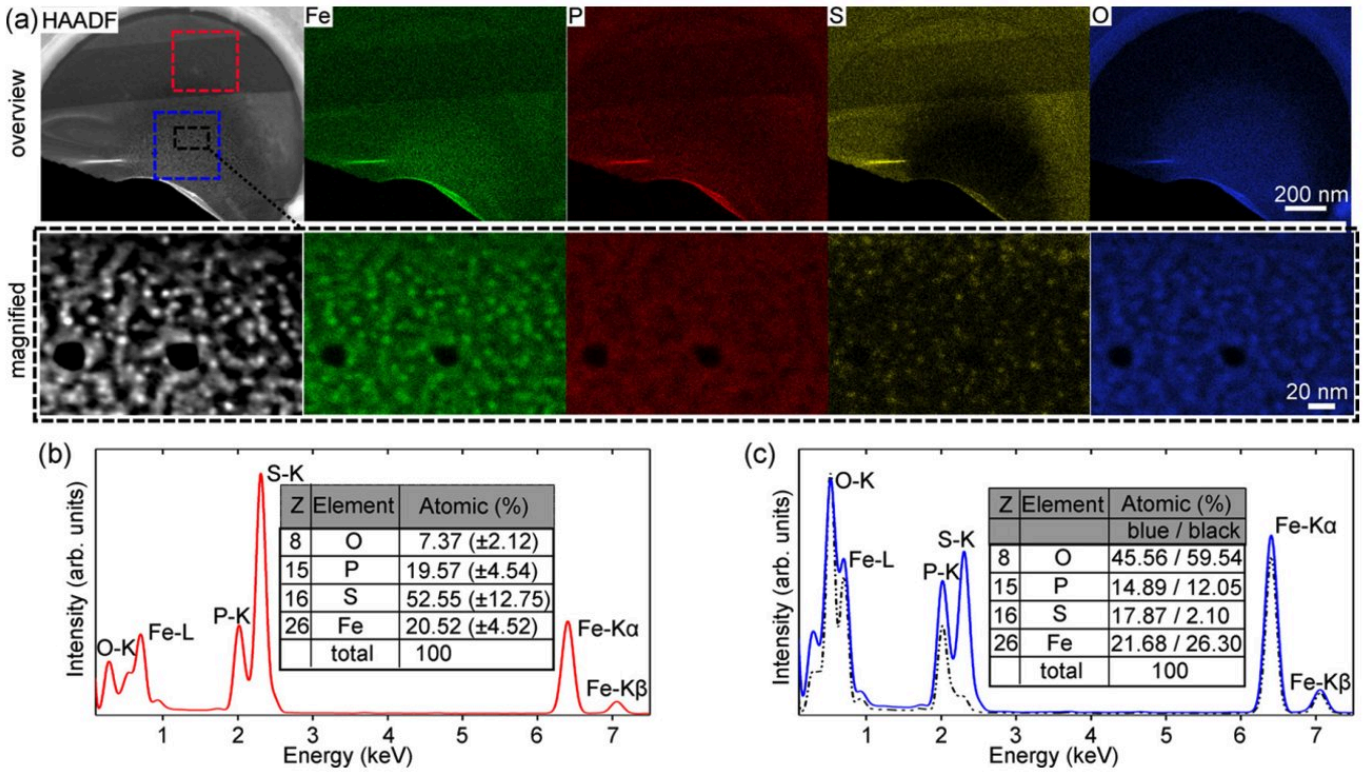

Fig. 5: HAADF image and Fe, P, S, O maps of few-layer $FePS_3$ with EDX spectra of pristine and irradiated regions.

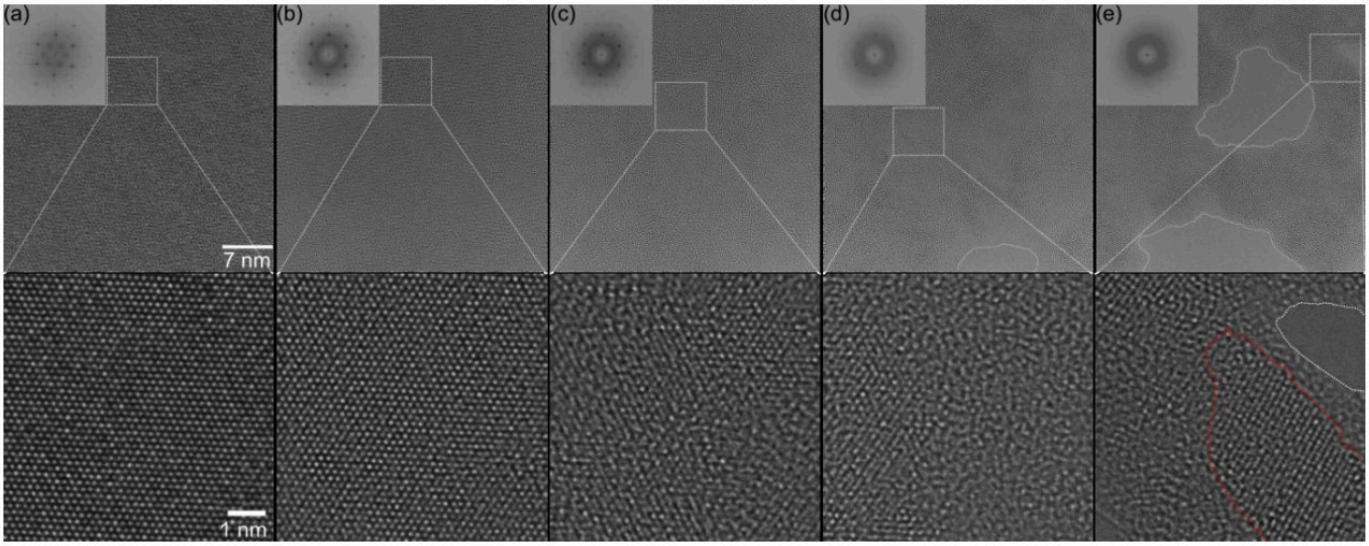

Fig. 6: 80 kV HRTEM series of $FePS_3$ under irradiation: vacancies, holes and clustered new phases.

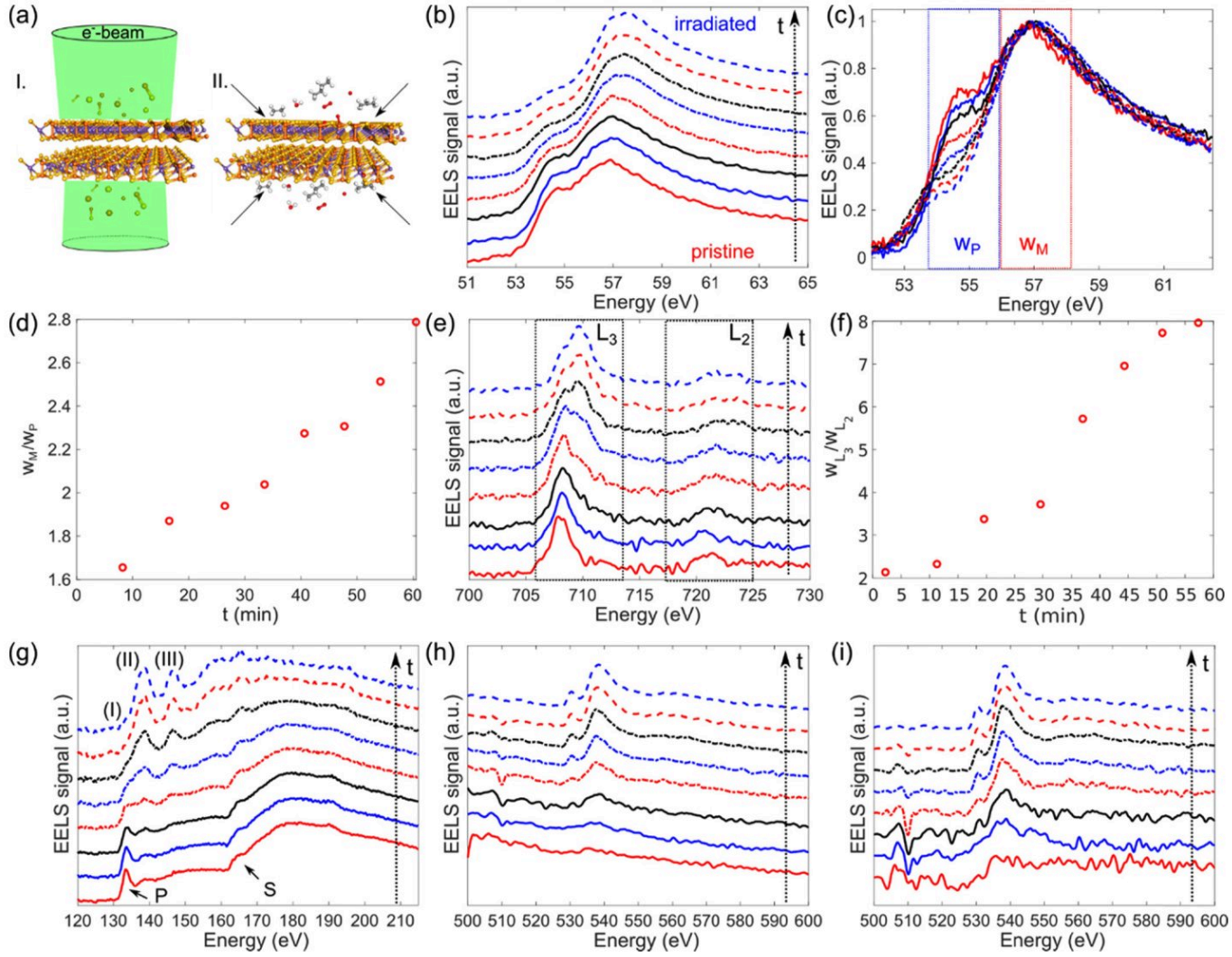

Fig. 7: Core-loss EELS of $FePS_3$ over time: Fe $M_{2,3}$ and $L_{2,3}$ edges turn Fe^{2+} into Fe^{3+}, P–S bonds break, oxygen accumulates.

Resource

Köster, J., Storm, A., Ghorbani-Asl, M., Kretschmer, S., Gorelik, T. E., Krasheninnikov, A. V., Kaiser, U. (2022).
Structural and Chemical Modifications of Few-Layer Transition Metal Phosphorous Trisulfides by Electron Irradiation.
J. Phys. Chem. C **126**(36), 15446–15455.
https://doi.org/10.1021/acs.jpcc.2c03800

References

1. Tang, K., Qi, W., Li, Y., Wang, T. (2018). Electronic Properties of van der Waals Heterostructure of Black Phosphorus and MoS2. *J. Phys. Chem. C*, **122**, 7027–7032. https://doi.org/10.1021/acs.jpcc.8b01476
2. Chowdhury, T., Sadler, E. C., Kempa, T. J. (2020). Progress and Prospects in Transition-Metal Dichalcogenide Research Beyond 2D. *Chem. Rev.*, **120**, 12563–12591. https://doi.org/10.1021/acs.chemrev.0c00505
3. Zhao, B., Shen, D., Zhang, Z., Lu, P., Hossain, M., Li, J., et al. (2021). 2D Metallic Transition-Metal Dichalcogenides: Structures, Synthesis, Properties, and Applications. *Adv Funct Materials*, **31**, 2105132. https://doi.org/10.1002/adfm.202105132
4. Gong, C., Zhang, Y., Chen, W., Chu, J., Lei, T., Pu, J., et al. (2017). Electronic and Optoelectronic Applications Based on 2D Novel Anisotropic Transition Metal Dichalcogenides. *Advanced Science*, **4**, 1700231. https://doi.org/10.1002/advs.201700231
5. Novoselov, K. S., Mishchenko, A., Carvalho, A., Castro Neto, A. H. (2016). 2D materials and van der Waals heterostructures. *Science*, **353**, aac9439. https://doi.org/10.1126/science.aac9439
6. Zhang, S., Liu, J., Kirchner, M. M., Wang, H., Ren, Y., Lei, W. (2021). Two-dimensional heterostructures and their device applications: progress, challenges and opportunities—review. *J. Phys. D: Appl. Phys.*, **54**, 433001. https://doi.org/10.1088/1361-6463/ac16a4
7. Li, L., Shang, Y., Lv, S., Li, Y., Fang, Y., Li, H. (2021). Flexible and highly responsive photodetectors based on heterostructures of MoS2 and all-carbon transistors. *Nanotechnology*, **32**, 315209. https://doi.org/10.1088/1361-6528/abf5ff
8. Wildes, A. R., Rule, K. C., Bewley, R. I., Enderle, M., Hicks, T. J. (2012). The magnon dynamics and spin exchange parameters of FePS3. *J. Phys.: Condens. Matter*, **24**, 416004. https://doi.org/10.1088/0953-8984/24/41/416004
9. Liu, J., Li, X. B., Wang, D., Lau, W. M., Peng, P., Liu, L. M. (2014). Diverse and tunable electronic structures of single-layer metal phosphorus trichalcogenides for photocatalytic water splitting. *The Journal of Chemical Physics*, **140**, 054707. https://doi.org/10.1063/1.4863695

10. Ismail, N., El-Meligi, A., Temerk, Y., Madian, M. (2010). Synthesis and characterization of layered FePS3 for hydrogen uptake. *International Journal of Hydrogen Energy*, **35**, 7827–7834. https://doi.org/10.1016/j.ijhydene.2010.05.061
11. Du, K. z., Wang, X. z., Liu, Y., Hu, P., Utama, M. I. B., Gan, C. K., et al. (2016). Weak Van der Waals Stacking, Wide-Range Band Gap, and Raman Study on Ultrathin Layers of Metal Phosphorus Trichalcogenides. *ACS Nano*, **10**, 1738–1743. https://doi.org/10.1021/acsnano.5b05927
12. Zhang, X., Zhao, X., Wu, D., Jing, Y., Zhou, Z. (2016). MnPSe3 Monolayer: A Promising 2D Visible-Light Photohydrolytic Catalyst with High Carrier Mobility. *Advanced Science*, **3**, 1600062. https://doi.org/10.1002/advs.201600062
13. Hashemi, A., Komsa, H. P., Puska, M., Krasheninnikov, A. V. (2017). Vibrational Properties of Metal Phosphorus Trichalcogenides from First-Principles Calculations. *J. Phys. Chem. C*, **121**, 27207–27217. https://doi.org/10.1021/acs.jpcc.7b09634
14. Jenjeti, R. N., Kumar, R., Austeria, M. P., Sampath, S. (2018). Field Effect Transistor Based on Layered NiPS3. *Sci Rep*, **8**, 8586. https://doi.org/10.1038/s41598-018-26522-1
15. Goossens, D. J. (2010). Dipolar anisotropy in quasi-2D honeycomb antiferromagnet MnPS3. *Eur. Phys. J. B*, **78**, 305–309. https://doi.org/10.1140/epjb/e2010-10569-x
16. Mayorga-Martinez, C. C., Sofer, Z., Sedmidubský, D., Huber, Š., Eng, A. Y. S., Pumera, M. (2017). Layered Metal Thiophosphite Materials: Magnetic, Electrochemical, and Electronic Properties. *ACS Appl. Mater. Interfaces*, **9**, 12563–12573. https://doi.org/10.1021/acsami.6b16553
17. Kim, T. Y., Park, C. H. (2021). Magnetic Anisotropy and Magnetic Ordering of Transition-Metal Phosphorus Trisulfides. *Nano Lett.*, **21**, 10114–10121. https://doi.org/10.1021/acs.nanolett.1c03992
18. Gibertini, M., Koperski, M., Morpurgo, A. F., Novoselov, K. S. (2019). Magnetic 2D materials and heterostructures. *Nat. Nanotechnol.*, **14**, 408–419. https://doi.org/10.1038/s41565-019-0438-6
19. Li, K., Chang, T., Xie, Q., Cheng, Y., Yang, H., Chen, J., et al. (2019). Tunable Magnetic Response in 2D Materials via Reversible Intercalation of Paramagnetic Ions. *Adv Elect Materials*, **5**, 1900040. https://doi.org/10.1002/aelm.201900040
20. Clement, R. (1980). A novel route to intercalation into layered MnPS3. J. Chem. Soc., Chem. *Commun.*, **647**. https://doi.org/10.1039/c39800000647
21. Spodine, E., Valencia-Gálvez, P., Manzur, J., Paredes-García, V., Pizarro, N., Bernot, K., et al. (2012). Optical properties of composites formed by transition metal macrocyclic complexes intercalated in thiophosphate layered phases. *Polyhedron*, **44**, 187–193. https://doi.org/10.1016/j.poly.2012.06.064
22. Spodine, E., Valencia-Gálvez, P., Fuentealba, P., Manzur, J., Ruiz, D., Venegas-Yazigi, D., et al. (2011). Magnetic behavior of MnPS3 phases intercalated by [Zn2L]2+ (LH2: macrocyclic ligand obtained by condensation of 2-hydroxy-5-methyl-1,3-benzenedicarbaldehyde and 1,2-diaminobenzene). *Journal of Solid State Chemistry*, **184**, 1129–1134. https://doi.org/10.1016/j.jssc.2011.03.009
23. Jana, R., Chowdhury, C., Datta, A. (2020). Transition-Metal Phosphorus Trisulfides and its Vacancy Defects: Emergence of a New Class of Anode Material for Li-Ion Batteries. *ChemSusChem*, **13**, 3855–3864. https://doi.org/10.1002/cssc.202001302
24. Wang, Y., Zhou, Z., Wen, T., Zhou, Y., Li, N., Han, F., et al. (2016). Pressure-Driven Cooperative Spin-Crossover, Large-Volume Collapse, and Semiconductor-to-Metal Transition in Manganese(II) Honeycomb Lattices. *J. Am. Chem. Soc.*, **138**, 15751–15757. https://doi.org/10.1021/jacs.6b10225
25. Yang, J., Zhou, Y., Guo, Q., Dedkov, Y., Voloshina, E. (2020). Electronic, magnetic and optical properties of MnPX3 (X = S, Se) monolayers with and without chalcogen defects: a first-principles study. *RSC Adv.*, **10**, 851–864. https://doi.org/10.1039/c9ra09030d
26. Murayama, C., Okabe, M., Urushihara, D., Asaka, T., Fukuda, K., Isobe, M., et al. (2016). Crystallographic features related to a van der Waals coupling in the layered chalcogenide FePS3. *Journal of Applied Physics*, **120**, 142114. https://doi.org/10.1063/1.4961712
27. Wildes, A. R., Okamoto, S., Xiao, D. (2021). Search for nonreciprocal magnons in MnPS3. *Phys. Rev. B*, **103**, 024424. https://doi.org/10.1103/physrevb.103.024424
28. Ju, H., Jeong, D. G., Choi, Y. G., Son, S., Jung, W. G., Jung, M. C., et al. (2020). Influence of stacking disorder on cross-plane thermal transport properties in TMPS3 (TM = Mn, Ni, Fe). *Applied Physics Letters*, **117**, 063103. https://doi.org/10.1063/5.0013107
29. Zhao, X., Kotakoski, J., Meyer, J. C., Sutter, E., Sutter, P., Krasheninnikov, A. V., et al. (2017). Engineering and modifying two-dimensional materials by electron beams. *MRS Bull.*, **42**, 667–676. https://doi.org/10.1557/mrs.2017.184
30. Dash, A. K., Swaminathan, H., Berger, E., Mondal, M., Lehenkari, T., Prasad, P. R., et al. (2023). Evidence of defect formation in monolayer MoS2 at ultralow accelerating voltage electron irradiation. *2D Mater.*, **10**, 035002. https://doi.org/10.1088/2053-1583/acc7b6
31. Björkman, T., Kurasch, S., Lehtinen, O., Kotakoski, J., Yazyev, O. V., Srivastava, A., et al. (2013). Defects in bilayer silica and graphene: common trends in diverse hexagonal two-dimensional systems. *Sci Rep*, **3**, 3482. https://doi.org/10.1038/srep03482
32. Cretu, O., Komsa, H. P., Lehtinen, O., Algara-Siller, G., Kaiser, U., Suenaga, K., et al. (2014). Experimental Observation of Boron Nitride Chains. *ACS Nano*, **8**, 11950–11957. https://doi.org/10.1021/nn5046147
33. Vasu, K. S., Prestat, E., Abraham, J., Dix, J., Kashtiban, R. J., Beheshtian, J., et al. (2016). Van der Waals pressure and its effect on trapped interlayer molecules. *Nat Commun*, **7**, 12168. https://doi.org/10.1038/ncomms12168
34. Köster, J., Ghorbani-Asl, M., Komsa, H. P., Lehnert, T., Kretschmer, S., Krasheninnikov, A. V., et al. (2021). Defect Agglomeration and Electron-Beam-Induced Local-Phase Transformations in Single-Layer MoTe2. *J. Phys. Chem. C*, **125**, 13601–13609. https://doi.org/10.1021/acs.jpcc.1c02202
35. Banhart, F., Kotakoski, J., Krasheninnikov, A. V. (2011). Structural Defects in Graphene. *ACS Nano*, **5**, 26–41. https://doi.org/10.1021/nn102598m
36. Zhou, W., Zou, X., Najmaei, S., Liu, Z., Shi, Y., Kong, J., et al. (2013). Intrinsic Structural Defects in Monolayer Molybdenum Disulfide. *Nano Lett.*, **13**, 2615–2622. https://doi.org/10.1021/nl4007479
37. Susi, T., Kotakoski, J., Kepaptsoglou, D., Mangler, C., Lovejoy, T. C., Krivanek, O. L., et al. (2014). Silicon–Carbon Bond Inversions Driven by 60-keV Electrons in Graphene. *Phys. Rev. Lett.*, **113**, 115501. https://doi.org/10.1103/physrevlett.113.115501
38. Luo, C., Wang, C., Wu, X., Zhang, J., Chu, J. (2017). In Situ Transmission Electron Microscopy Characterization and Manipulation of Two-Dimensional Layered Materials beyond Graphene. *Small*, **13**, 1604259. https://doi.org/10.1002/smll.201604259
39. Lehnert, T., Ghorbani-Asl, M., Köster, J., Lee, Z., Krasheninnikov, A. V., Kaiser, U. (2019). Electron-Beam-Driven Structure Evolution of Single-Layer MoTe2 for Quantum Devices. *ACS Appl. Nano Mater.*, **2**, 3262–3270. https://doi.org/10.1021/acsanm.9b00616
40. Komsa, H. P., Kotakoski, J., Kurasch, S., Lehtinen, O., Kaiser, U., Krasheninnikov, A. V. (2012). Two-Dimensional Transition Metal Dichalcogenides under Electron Irradiation: Defect Production and Doping. *Phys. Rev. Lett.*, **109**, 035503. https://doi.org/10.1103/physrevlett.109.035503
41. Lehnert, T., Lehtinen, O., Algara–Siller, G., Kaiser, U. (2017). Electron radiation damage mechanisms in 2D MoSe2. *Applied Physics Letters*, **110**, 033106. https://doi.org/10.1063/1.4973809
42. Zhang, J., Yu, Y., Wang, P., Luo, C., Wu, X., Sun, Z., et al. (2019). Characterization of atomic defects on the photoluminescence in two-dimensional materials using transmission electron microscope. *InfoMat*, **1**, 85–97. https://doi.org/10.1002/inf2.12002
43. Köster, J., Liang, B., Storm, A., Kaiser, U. (2021). Polymer-assisted TEM specimen preparation method for oxidation-sensitive 2D materials. *Nanotechnology*, **32**, 075704. https://doi.org/10.1088/1361-6528/abc49e
44. Kretschmer, S., Lehnert, T., Kaiser, U., Krasheninnikov, A. V. (2020). Formation of Defects in Two-Dimensional MoS2 in the Transmission Electron Microscope at Electron Energies below the Knock-on Threshold: The Role of Electronic Excitations. *Nano Lett.*, **20**, 2865–2870. https://doi.org/10.1021/acs.nanolett.0c00670
45. Ouvrard, G., Brec, R., Rouxel, J. (1985). Structural determination of some MPS3 layered phases (M = Mn, Fe, Co, Ni and Cd). *Materials Research Bulletin*, **20**, 1181–1189. https://doi.org/10.1016/0025-5408(85)90092-3

46. Malis, T., Cheng, S. C., Egerton, R. F. (1988). EELS log-ratio technique for specimen-thickness measurement in the TEM. *J. Elec. Microsc. Tech.*, **8**, 193–200. https://doi.org/10.1002/jemt.1060080206
47. de Graaf, S., Kooi, B. J. (2022). Radiation damage and defect dynamics in 2D WS2: a low-voltage scanning transmission electron microscopy study. *2D Mater.*, **9**, 015009. https://doi.org/10.1088/2053-1583/ac3377
48. de Graaf, S., Ahmadi, M., Lazić, I., Bosch, E. G. T., Kooi, B. J. (2021). Imaging atomic motion of light elements in 2D materials with 30 kV electron microscopy. *Nanoscale*, **13**, 20683–20691. https://doi.org/10.1039/d1nr06614e
49. Susi, T., Meyer, J. C., Kotakoski, J. (2019). Quantifying transmission electron microscopy irradiation effects using two-dimensional materials. *Nat Rev Phys*, **1**, 397–405. https://doi.org/10.1038/s42254-019-0058-y
50. Egerton, R. (2021). Radiation Damage and Nanofabrication in TEM and STEM. *Micros. Today*, **29**, 56–59. https://doi.org/10.1017/s1551929521000663
51. Chen, F. R., Van Dyck, D., Kisielowski, C., Hansen, L. P., Barton, B., Helveg, S. (2021). Probing atom dynamics of excited Co-Mo-S nanocrystals in 3D. *Nat Commun*, **12**, 5007. https://doi.org/10.1038/s41467-021-24857-4
52. Kisielowski, C., Specht, P., Rozeveld, S. J., Kang, J., Fielitz, A. J., Barton, D., et al. (2021). Modulating Electron Beam–Sample Interactions in Imaging and Diffraction Modes by Dose Fractionation with Low Dose Rates. *Microscopy and Microanalysis*, **27**, 1420–1430. https://doi.org/10.1017/S143192762101268X
53. Meyer, J. C., Eder, F., Kurasch, S., Skakalova, V., Kotakoski, J., Park, H. J., et al. (2012). Accurate Measurement of Electron Beam Induced Displacement Cross Sections for Single-Layer Graphene. *Phys. Rev. Lett.*, **108**, 196102. https://doi.org/10.1103/PhysRevLett.108.196102
54. McKinley, W. A., Feshbach, H. (1948). The Coulomb Scattering of Relativistic Electrons by Nuclei. *Phys. Rev.*, **74**, 1759–1763. https://doi.org/10.1103/physrev.74.1759
55. Mott, N. F. (1929). The scattering of fast electrons by atomic nuclei. Proceedings of the Royal Society of London. Series A, Containing Papers of a Mathematical and Physical Character, 124, 425–442. https://doi.org/10.1098/rspa.1929.0127
56. Susi, T., Hofer, C., Argentero, G., Leuthner, G. T., Pennycook, T. J., Mangler, C., et al. (2016). Isotope analysis in the transmission electron microscope. *Nat Commun*, **7**, 13040. https://doi.org/10.1038/ncomms13040
57. Komsa, H. P., Krasheninnikov, A. V. (2012). Effects of confinement and environment on the electronic structure and exciton binding energy of MoS2 from first principles. *Phys. Rev. B*, **86**, 241201. https://doi.org/10.1103/physrevb.86.241201
58. Joseph, T., Ghorbani-Asl, M., Kvashnin, A. G., Larionov, K. V., Popov, Z. I., Sorokin, P. B., et al. (2019). Nonstoichiometric Phases of Two-Dimensional Transition-Metal Dichalcogenides: From Chalcogen Vacancies to Pure Metal Membranes. *J. Phys. Chem. Lett.*, **10**, 6492–6498. https://doi.org/10.1021/acs.jpclett.9b02529
59. Brec, R. (1986). Review on structural and chemical properties of transition metal phosphorus trisulfides MPS3. In: Intercalation in Layered Materials, pp. 93–124. Springer, Boston, MA. https://doi.org/10.1007/978-1-4757-5556-5_4
60. van Aken, P. A., Styrsa, V. J., Liebscher, B., Woodland, A. B., Redhammer, G. J. (1999). Microanalysis of Fe3+/ΣFe in oxide and silicate minerals by investigation of electron energy-loss near-edge structures (ELNES) at the Fe M 2,3 edge. *Physics and Chemistry of Minerals*, **26**, 584–590. https://doi.org/10.1007/s002690050222
61. Tan, H., Verbeeck, J., Abakumov, A., Van Tendeloo, G. (2012). Oxidation state and chemical shift investigation in transition metal oxides by EELS. *Ultramicroscopy*, **116**, 24–33. https://doi.org/10.1016/j.ultramic.2012.03.002
62. van Aken, P. A., Liebscher, B., Styrsa, V. J. (1998). Quantitative determination of iron oxidation states in minerals using Fe L2,3-edge electron energy-loss near-edge structure spectroscopy. *Physics and Chemistry of Minerals*, **25**, 323–327. https://doi.org/10.1007/s002690050122
63. van Aken, P. A., Liebscher, B. (2002). Quantification of ferrous/ferric ratios in minerals: new evaluation schemes of Fe L2,3 electron energy-loss near-edge spectra. *Physics and Chemistry of Minerals*, **29**, 188–200. https://doi.org/10.1007/s00269-001-0222-6
64. Garvie, L., Craven, A. (1994). High-resolution parallel electron energy-loss spectroscopy of Mn L2,3-edges in inorganic manganese compounds. *Phys Chem Minerals*, **21**. https://doi.org/10.1007/bf00202132
65. Schmid, H., Mader, W. (2006). Oxidation states of Mn and Fe in various compound oxide systems. *Micron*, **37**, 426–432. https://doi.org/10.1016/j.micron.2005.12.004
66. Lau, W. M., Jin, S., Wu, X. W., Ingrey, S. (1990). In situ x-ray photoelectron spectroscopic study of remote plasma enhanced chemical vapor deposition of silicon nitride on sulfide passivated InP. *Journal of Vacuum Science & Technology B: Microelectronics Processing and Phenomena*, **8**, 848–855. https://doi.org/10.1116/1.584977
67. Kruse, J., Leinweber, P., Eckhardt, K. U., Godlinski, F., Hu, Y., Zuin, L. (2009). Phosphorus L2,3-edge XANES: overview of reference compounds. *J Synchrotron Rad*, **16**, 247–259. https://doi.org/10.1107/s0909049509000211